Acta Materialia 174 (2019) 398–405

Contents lists available at ScienceDirect

Acta Materialia

journal homepage: www.elsevier.com/locate/actamat

Full length article

Electron-configuration stabilized $(W,Al)B_2$ solid solutions

Rainer Hahn [a, *], Vincent Moraes [a], Andreas Limbeck [b], Peter Polcik [c], Paul H. Mayrhofer [a], Holger Euchner [a, d]

[a] Institute of Materials Science and Technology, TU Wien, 1060, Vienna, Austria
[b] Institute of Chemical Technologies and Analytics, TU Wien, 1060, Vienna, Austria
[c] Plansee Composite Materials GmbH, 86983, Lechbruck am See, Germany
[d] Helmholtz Institute for Electrochemical Energy Storage, 89081, Ulm, Germany

ARTICLE INFO

Article history:
Received 1 March 2019
Received in revised form
16 May 2019
Accepted 26 May 2019
Available online 29 May 2019

Keywords:
Thin films
Borides
Sputtering
Vacancies
Density functional theory

ABSTRACT

By combining experimental and theoretical methods, we have conducted a detailed study of the ternary diboride system $(W_{1-x}Al_x)_{1-y}B_{2(1-z)}$. Tungsten rich solid solutions of $(W_{1-x}Al_x)_{1-y}B_{2(1-z)}$ were synthesized by physical vapor deposition and subsequently investigated for structure, mechanical properties and thermal stability. All crystalline films show hardness values above 35 GPa, while the highest thermal stability was found for low Al contents. In this context, the impact of point defects on the stabilization of the AlB_2 structure type is investigated, by means of ab initio methods. Most notably, we are able to show that vacancies on the boron sublattice are detrimental for the formation of Al-rich $(W_{1-x}Al_x)_{1-y}B_{2(1-z)}$, thus providing an explanation why only tungsten rich phases are crystalline.

1. Introduction

Nowadays the increasing interest in sustainability also results in a growing industrial demand for protective coatings with superior mechanical properties such as high hardness, good elastic properties, and improved thermal stability. As a consequence, the search for improved physical properties leads to the exploration of new material systems. Despite the fact that transition metal (TM) based nitrides are successfully applied in automotive or aerospace industries, the quest for improved functional materials is an ongoing challenge [1–3].

One of the peculiarities of vapor phase deposition techniques is the fact that they allow the growth of supersaturated non-equilibrium phases like cubic $Ti_{1-x}Al_xN$ (NaCl-prototype, $Fm\bar{3}m$, space group 225). Here, the supersaturation of the cubic TiN phase essentially starts with small aluminum contents [4] leading to $Ti_{1-x}Al_xN$ solid solutions. A further increase of the Al fraction causes a further supersaturation of the cubic phase, which is found to result in age hardening effects at elevated temperatures. The origin of this age hardening is found in the spinodal decomposition of cubic $Ti_{1-x}Al_xN$, which goes along with the formation of TiN- and AlN-rich cubic domains [5–8]. A degradation of the mechanical properties may only occur under further annealing when the metastable cubic AlN transforms into the thermodynamically stable wurtzite phase. A major retarding force for this phase transformation arises from the associated huge volume increase of almost 30% [7]. However, the significant volume change going along with this cubic to wurtzite transition may trigger toughening effects for controlled AlN phase fractions [9–11]. Consequently, the exceptional properties of $Ti_{1-x}Al_xN$ can be attributed to the interplay and competition of the two boundary phases—cubic TiN and wurtzite AlN—which prefer to crystallize in different structure types.

This well-known concept, being responsible for the unique properties of $Ti_{1-x}Al_xN$ and its derivatives, has lately been evoked as design principle for ternary borides, opening access to this new class of functional materials with various exceptional properties such as improved mechanical properties and enhanced thermal stability [12–17]. Despite the large progress that has been achieved with such concepts for ternary and even quaternary TM nitrides, the field of multinary borides is still largely unexplored and also lacks fundamental understanding.

Many diborides, comprising the technologically relevant TiB_2 phase [18,19], have been observed to crystallize in the so-called α-

* Corresponding author. Institute of Materials Science and Technology, TU Wien, Getreidemarkt 9/E308, A-1060, Vienna, Austria.
E-mail address: rainer.hahn@tuwien.ac.at (R. Hahn).

https://doi.org/10.1016/j.actamat.2019.05.056

type structure [20], with a three atom unit cell of space group 191 (AlB_2-prototype, *P6/mmm*) [21]. This structure type can be illustrated as a stacking of boron planes (the boron atoms form covalently bonded hexagons) separated by hexagonal metal planes as given in Fig. 1. The boron atoms sit in every vertex formed by three neighboring metal atoms (or in other words, the metal atoms are always in the center of a hexagon formed by the boron atoms). Apart from the prevailing α-type modification, other binary boride phases are known to adopt slightly different crystal structures. WB_2 is observed to crystallize in at least two different modifications [22,23]. Physical vapor deposited WB_2 thin films have been reported to crystallize in the α-type [24,25] structure, whereas bulk materials prefer the so-called ω modification, also known as W_2B_{5-z}-prototype [23]. The ω-phase is closely related to the AlB_2-prototype, however, it consists of alternating flat and puckered boron layers. Still the boron atoms form covalently bonded hexagons (either flat or puckered) and the metal atoms form flat hexagonal planes. In Fig. 1 it is also apparent that the position ("stacking" on the metal sublattice) of the hexagonal metal-planes changes due to the puckered boron plane (*i.e.* from the "A" site to the "B" site and then back to again to the "A" site with the next puckered plane – using the well-known notification of AB stacking of densely packed layer in hexagonal close packed structures). As a consequence of the alternating layers an increased unit cell, comprising twelve atoms and adapting space group 194 (*P63/mmc*), is necessary to describe the ω-modification, as presented in Fig. 1.

Here, $(W_{1-x}Al_x)_{1-y}B_{2(1-z)}$ thin films with varying Al metal fractions x up to 50.1 at% on the metal sublattice have been deposited using physical vapor deposition (PVD). The obtained films reveal a high hardness, with the maximum value reaching almost 42 GPa for the case of WB_{2-z}. Furthermore, high thermal stability was observed with the films remaining stable after 30 min of annealing at 1000 °C. Decomposition and stabilization of α-$(W_{1-x}Al_x)_{1-y}B_{2(1-z)}$ is investigated by ab initio methods, once more pointing out the importance of point defects for the phase evolution of PVD deposited materials [13,26,27] and most strikingly giving an explanation for the fact that it is extremely difficult to grow Al-rich ternary boride thin films. In fact, a detailed literature review showed that there is no report about a crystalline AlB_2 thin film in the as deposited state. Nevertheless, the addition of Al to WB_2 will promote their self-passivating effects, as observed for Al alloying in ReB_2 [28].

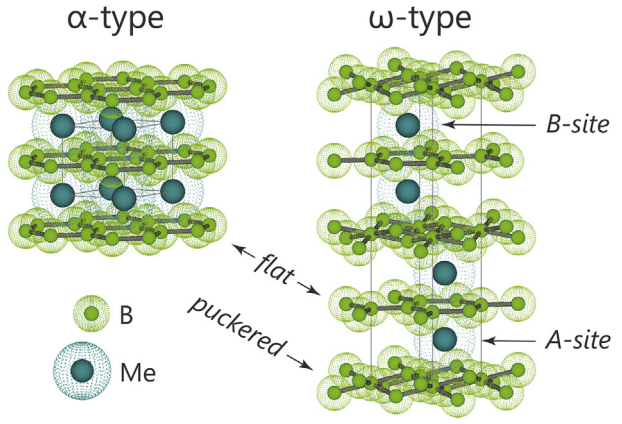

Fig. 1. Structure of the α-AlB_2 and ω-W_2B_{5-z} prototypes with the corresponding layer sequence.

2. Experimental and computational methods

A lab-scale magnetron sputtering system (AJA Orion 5) was used to deposit ternary $(W_{1-x}Al_x)_{1-y}B_{2(1-z)}$ films with varying Al content (the base pressure was below 0.1 mPa). Two diboride targets, namely a 2-inch W_2B_{5-z} and a 2-inch AlB_2 target (Plansee Composite Materials GmbH), were operated by dc plasma generators with a power-controlled signal. The maximum target power density was set to 7.4 $W \cdot cm^{-2}$ and accordingly reduced for chemical variations. In our setup, the magnetrons, in a dual confocal arrangement, face the rotating substrate holder, which is placed at a distance of 11 cm. After reaching a temperature of 500 °C, single crystalline Si (100-oriented) and sapphire substrates ($1\bar{1}02$-oriented) were ion etched in Ar atmosphere (at a pressure of 6 Pa). During the depositions, the substrate temperature was kept constant at a temperature of 500 °C, while a working gas pressure (Ar) of 0.7 Pa was used and no bias voltage was applied (the floating potential is about −20 V). We had to reduce the working gas pressure to 0.4 Pa for obtaining close to stoichiometric WB_2 films, because with 0.7 Pa we ended up with a $WB_{1.4}$ film. A similar dependence of the B/metal ratio on the working gas pressure was reported for TiB_x [29]. The deposition time was 240 min resulting in 1.1–1.8 μm thin films, depending on the power density of the W_2B_{5-z} target and working gas pressure used (resulting in a typical deposition rate of 6 $nm \cdot min^{-1}$). The high Al-containing thin film was deposited for 480 min to obtain a comparable thickness.

The elemental composition of the as-deposited thin films on Si substrates was determined by inductively coupled plasma atomic emission spectroscopy (ICP-AES), for dissolution samples were treated with a mixture of nitric acid and hydrofluoric acid at elevated temperature [30]. This method was chosen since it allows for an accurate determination of the boron content, which is difficult to access by other characterization techniques. Structure and morphology of the as-deposited films on sapphire substrates were investigated by X-ray diffraction (XRD).

The thermal stability was investigated by comparing XRD measurements of the thin films in as-deposited state and after annealing (base pressure below 0.1 mPa) at 1000 °C for 30 min in He atmosphere (the heating rate was 20 K/min and the cooling rate by simply turning off the heater was >50 K/min down to 500 °C). XRD measurements were conducted with a PANalytical XPert Pro MPD (θ-θ diffractometer) in Bragg Brentano geometry equipped with a CuK_α cathode (wave length $\lambda = 1.54$ Å, 45 kV, 40 mA).

Moreover, a FEI Quanta 250 scanning electron microscope equipped with a field emission gun (FEGSEM) was used to take cross section micrographs. The residual stresses of our thin films were determined using the Stoney-equation [31], after extracting the substrate curvature making use of a Nanovea PS50 chromatic confocal profilometer.

The mechanical properties of both, the as-deposited and the annealed coatings on sapphire substrates, were studied by nanoindentation, using an ultra-micro indentation system (UMIS). Loads within a range from 3 to 45 mN were applied with a Berkovich type indenter. Indents exceeding an indentation depth greater than 10% of the film thickness were excluded from the analysis to minimize the substrate interference. Hardness and indentation modulus were determined from the resulting load-displacement curves of the nanoindents using the standard approach after Oliver and Pharr [32], the errors noted are standard deviations.

The structural stability of α- and ω-$(W_{1-x}Al_x)_{1-y}B_{2(1-z)}$ with respect to stoichiometry and changing vacancy concentrations on the respective sublattice y and z was investigated by means of density functional theory (DFT). For this purpose the Vienna Ab Initio Simulation Package (VASP) [33,34], using the projector augmented wave method [35], was applied. Exchange and

correlation were accounted for by the generalized gradient approximation as introduced by Perdew and Wang [36]. To start with, supercells of the α- and the ω-modification of $(W_{1-x}Al_x)_{1-y}B_{2(1-z)}$ were constructed. For the smaller α-phase a $2 \times 2 \times 4$ supercell, containing 48 atoms, was selected, whereas in case of ω-$(W_{1-x}Al_x)_{1-y}B_{2(1-z)}$ a $2 \times 2 \times 1$ supercell with the same number of atoms was created. For the realization of solid solutions or random alloys with different stoichiometries the metal sublattices were populated by the respective Al/W ratios, by making use of the special quasirandom structure (SQS) approach [37]. The corresponding SQS structures were then constructed using the at package [38]. As a next step, atomic coordinates and lattice geometry of the obtained SQS configurations were optimized using the VASP code with an energy cutoff of 600 eV and a $8 \times 8 \times 4$ Γ-centered k-point mesh. The plane wave cutoff energy and the k-point resolution were chosen to ensure convergence and an accuracy of the calculation within a few meV/at. To introduce vacancies in the two structure types, the same approach was used by simply considering vacancies as additional alloying element in the SQS approach.

Schematics were produced using VESTA [39].

3. Results and discussion

Solid solutions of $(W_{1-x}Al_x)_{1-y}B_{2(1-z)}$ thin films have been prepared for various Al/W ratios, evidencing boron contents between 60 and 66%, thus being close to stoichiometric $(W_{1-x}Al_x)_{1-y}B_{2(1-z)}$ diborides (see Table 1).

Our XRD results highlight that only for Al metal fractions far below 50 at%, as-deposited crystalline films can be obtained (see Fig. 2). For Al metal fractions below 20% (*i.e.*, $x \leq 0.2$), we clearly see single phase solid solution of α-$(W_{1-x}Al_x)_{1-y}B_{2(1-z)}$ with the c-axis lattice parameters lying in between those of α-AlB_2 [40] and the experimentally observed one of α-WB_2 [22]. With increasing Al content, the positions of the (001) and (002) reflections shift to lower angles also confirming the incorporation of Al on the metal sublattice.

In agreement with these XRD investigations, the fracture cross sectional SEM micrographs, Fig. 3, show dense columnar growth morphologies for all thin films, except the highest Al-containing one. The cross section of the latter is more comparable to amorphous-like films. Additionally, an increased growth rate when reducing the deposition pressure is seen for the binary WB_2-based thin film.

Interestingly, our $(W_{1-x}Al_x)_{1-y}B_{2(1-z)}$ thin films exhibit significant changes in their XRD patterns upon 30-min annealing in He atmosphere at 1000 °C. The initially amorphous film with an Al fraction of 50.1 at% on the metal sublattice (absolute Al content of 17.3 at%) shows clearly crystalline XRD peaks at the position of ω-W_2B_{5-z} [41]. The (nano-) crystals of this coating are randomly oriented (contrary to our other thin films) and they crystallize in the ω-type structure. For the film with 19.2 at% Al on the metal sublattice (absolute Al content of 6.9 at%), we observe a peak splitting of the (002) reflection upon annealing, which will also be discussed in the DFT section. This peak-splitting points to a spinodal decomposition of our $W_{0.81}Al_{0.19}B_2$ film towards a less defected Al-enriched $W_{0.81-\xi}Al_{0.19+\xi}B_2$ (ξ indicates an increased Al content and a decreased W content) phase and a vacancy containing W-enriched WB_{2-z} phase. All other films show no signs of decomposition, but also a shift of the major XRD peaks (001) and (002) towards higher 2θ angles indicating recovery events (where structural defects rearrange towards lower energy sites, leading to a relief of microstrains).

The amorphous film—based on previous studies showing that sputtering of AlB_2 targets leads to amorphous films, we correlate this to the high Al content—shows a hardness of 24 GPa and an indentation modulus of 341 GPa. Both values are considerably lower than those of our crystalline materials. For the whole composition range, the hardness values of the crystalline α-$(W_{1-x}Al_x)_{1-y}B_{2(1-z)}$ thin films lie above 35 GPa, with the maximum of 42 ± 2 GPa for the binary α-WB_2 thin film (see Table 1). A noteworthy trend is the decreasing hardness with increasing Al content. This decrease in hardness of our $(W_{1-x}Al_x)_{1-y}B_{2(1-z)}$ thin films can be attributed to reduced bond strengths, mirrored also by decreasing indentation moduli. The residual stresses of our thin films are given in Table 1, we observe a decrease with increasing Al-content. The hardness of our thin films on Si substrates is ~1 GPa lower than on sapphire substrates, which can be attributed to lower residual compressive stresses on Si (~0.9 GPa, resulting from differences in the thermal expansion coefficients of the substrate materials). Also, the Young's modulus yields slightly lower values on Si than on sapphire substrates (however, well within the experimental error), which can again be attributed to the influence of residual stresses. The elastic recovery of our coatings varied between 61 and 63%, with a trend to higher recovery at lower Al contents, an exception was found for the initially amorphous film, where the recovery was only 53%. The mechanical properties of the annealed samples (1000 °C for 30 min) are listed in Table 1. Due to delamination of the binary α-WB_{2-z} thin film during annealing, no H and E^* could be obtained from this sample in the annealed state. Also $(W_{1-x}Al_x)_{1-y}B_{2(1-z)}$ thin films with Al metal fractions of 9.7 and 19.2 at% showed a significant crack pattern after annealing. However, the initially amorphous $W_{0.50}Al_{0.50}B_2$ thin film showed no crack formation during annealing, allowing to measure their mechanical properties to be $H = 28$ GPa and $E^* = 407$ GPa, hence, higher than in the as deposited state.

Ab initio calculations for $(W_{1-x}Al_x)_{1-y}B_{2(1-z)}$ predict the α-phase to become energetically more stable when the Al population on the metal sublattice exceeds ~50%, considering any types of vacancies

Table 1
Hardness H, indentation moduli E^*, elastic recovery ε_R, and residual stress σ_R of $(W_{1-x}Al_x)_{1-y}B_{2(1-z)}$ thin films depicted with respect to the sputtering power ratio, film thickness, and the chemical composition before and after annealing at 1000 °C in He atmosphere. All errors are standard deviations.

Sputtering-power ratio AlB_2/W_2B_{5-z} (−)	Film thickness h (μm)	Chemical composition (at%)				Mechanical properties (Sapphire substrate)					
						As deposited				Annealed 1000 °C	
		Al	W	B	$\frac{Al}{Al+W}$	H (GPa)	E^* (GPa)	ε_R (%)	σ_R (GPa)	H (GPa)	E^* (GPa)
0.0(0/150)	1.8	0.0	35.0 ± 0.2	65.0 ± 0.2	0	42 ± 2	593 ± 12	63 ± 2	−1.5 ± 0.1	*	
0.5 (75/150)	1.5	0.9 ± 0.1	38.9 ± 0.2	60.2 ± 0.1	2.3	39 ± 1	550 ± 35	63 ± 2	−1.1 ± 0.1	37 ± 2	559 ± 15
1.0 (150/150)	1.7	3.6 ± 0.2	34.0 ± 0.2	62.4 ± 0.1	9.7	38 ± 2	494 ± 31	63 ± 2	−0.7 ± 0.1	(35 ± 2)	†
2.0 (150/75)	1.1	6.9 ± 0.1	29.1 ± 0.1	64.0 ± 0.1	19.2	36 ± 1	459 ± 29	62 ± 2	−0.6 ± 0.1	‡	
4.0 (150/38)	1.8	17.3 ± 1.0	17.3 ± 0.3	65.4 ± 1.3	50.1	24 ± 1	341 ± 7	53 ± 2	−1.2 ± 0.1	28 ± 2	407 ± 24

* delamination due to compressive stresses.
† little crack formation during annealing.
‡ crack formation during annealing.

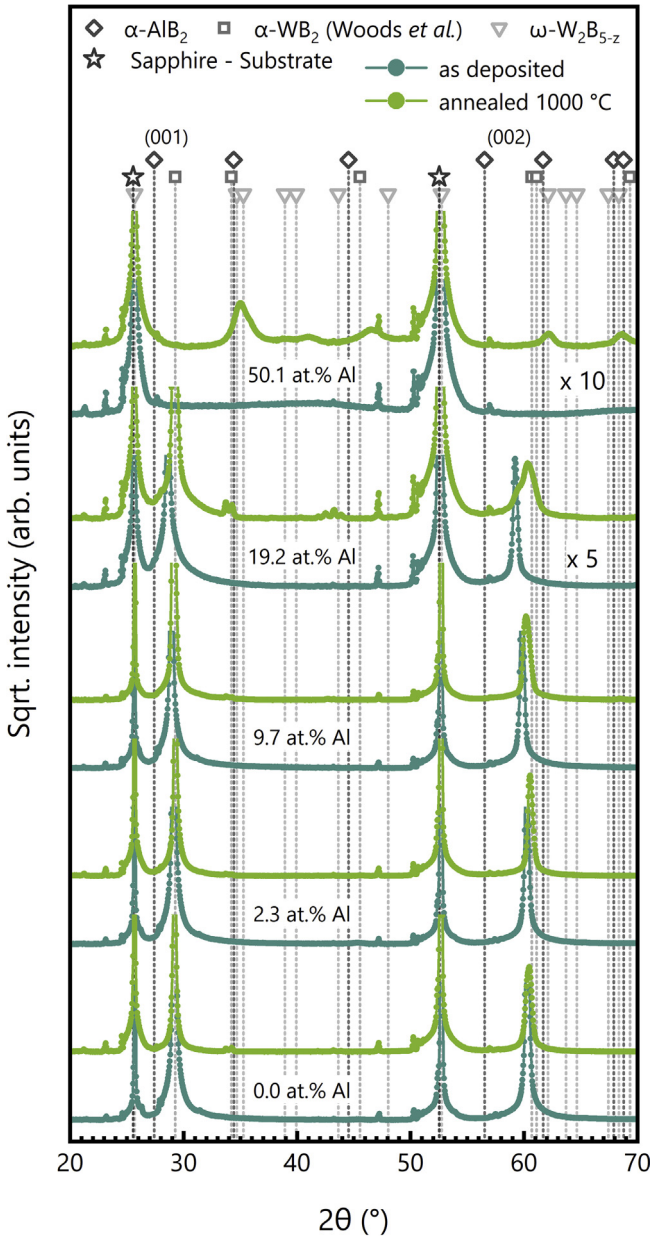

Fig. 2. XRD patterns of as deposited (blue) and annealed (green) $W_{1-x}Al_xB_2$ thin films. The symbols with vertical lines represent diffraction peak positions of α-AlB_2. α-WB_2 and ω-W_2B_{5-z}. Substrate reflections are also indicated. The XRD patterns of the films containing an Al metal fraction of 19.2 and 50.1 are presented with 5 times respectively 10 times their intensity. (For interpretation of the references to color in this figure legend, the reader is referred to the Web version of this article.)

[12]. However, experimentally the α-phase is unambiguously observed for all our crystalline thin films. This is in good agreement with other recent PVD studies [13,24,25], which report that even the binary WB_2 crystallizes in the α modification. As PVD methods are known to promote the incorporation of point defects—such as vacancies—during crystal growth, detailed ab initio studies on the impact of point defects on crystal structure and energy of formation have been performed, suggesting that these are the major reasons for the stabilization of WB_2 (and also other diborides) in its metastable α-structure [13,42].

To study the consequences of an increased vacancy concentration on the phase stability of ternary $(W_{1-x}Al_x)_{1-y}B_{2(1-z)}$ we have analyzed the energy of formation, E_f, of both, the α-type and the ω-type modification, for changing chemical compositions and concentrations of vacancies, following eqn. (1):

$$E_f = \frac{1}{\sum_i n_i}\left(E_{tot} - \sum_i n_i E_i\right) \quad (1)$$

here, E_{tot} and E_i gives the total energy of the alloy and its elemental constituents, as obtained from DFT, whereas n_i denotes the number of atoms of a given species *i*. In case of $(W_{1-x}Al_x)_{1-y}B_{2(1-z)}$ the energy of formation is a measure for the energy gain when an $(W_{1-x}Al_x)_{1-y}B_{2(1-z)}$ alloy is formed from fcc-Al, bcc-W and α-B.

In perfect agreement with earlier results [13], we find WB_2 to be more stable in the ω-phase, whereas AlB_2 prefers the α structure type. However, by including vacancies, the α-phase of WB_2 can indeed be shown to become energetically more favorable [43]. To further interpret our diffraction patterns, we have investigated the evolution of the lattice parameter for the α-phase of AlB_2 and WB_2 with different vacancy concentrations (see Table 2.)

The calculations clearly show that for defect-free crystals, the c-axis lattice parameter of α-WB_2 is actually larger than that one of α-AlB_2. Thus, the c-axis lattice parameter would decrease with decreasing W content for defect-free α-$(W_{1-x}Al_x)_{1-y}B_{2(1-z)}$ solid solutions, causing a shift of the (001) reflection to higher diffraction angles. However, the opposite effect is observed in our XRD patterns. Again, the incorporation of vacancies in our crystalline structures (due to the PVD process) can account for this behavior. Table 2 clearly shows that the difference in c-axis lattice parameters between α-WB_2 and α-AlB_2 decreases with increasing vacancy content. Finally, in case of $M_{0.875}B_{1.75}$ (*i.e.*, 12.5% Schottky defects) the c-axis lattice parameter of the defected α-WB_2 becomes smaller than that of the defected α-AlB_2 thus being significantly smaller than that of defect-free α-AlB_2 which is in perfect agreement to our previous study [42]. Consequently, the combination of experimental and computational studies strongly points towards an increased vacancy concentration in our PVD films. Moreover, the overall residual stresses can be ruled out as origin of a peak shift in our XRD measurements, as the trend in σ_R would cause a shift in the opposite direction.

The impact of vacancies on the phase stability of $(W_{1-x}Al_x)_{1-y}B_{2(1-z)}$ is indeed striking, as detailed in Fig. 4a. In this figure we show the energy of formation with respect to the chemical composition for defect-free α- and ω-$(W_{1-x}Al_x)_{1-y}B_{2(1-z)}$, and compare it to structures with incorporated metal and boron vacancies. The results clearly point out that the formation of B vacancies, Me vacancies, as well as B and Me vacancies, lead to more positive E_f values for ω-structured $(W_{1-x}Al_x)_{1-y}B_{2(1-z)}$ solid solutions across the entire x range (generally, the E_f-vs-x curve for ω-$(W_{1-x}Al_x)_{1-y}B_{2(1-z)}$ moves upwards when defects are included, Fig. 4a, slightly more on the W-rich side). Consequently, the formation of vacancies is energetically penalized in the ω-phase.

The impact on the α-phase is different. The formation of B, Me, as well as B and Me vacancies leads to more negative E_f values for W-rich solid solutions. The Al-rich part, especially for $x = 1$, only shows slightly more negative E_f values if a small amount of Me vacancies is considered (E_f is slightly more negative for α-$Al_{0.9375}B_2$ than α-AlB_2, Table 2). The formation of boron vacancies is strongly penalized, leading to E_f values close to zero for $AlB_{1.9375}$ or even positive for higher B-vacancy concentrations (Table 2). Consequently, the formation of B and Me vacancies (especially in form of Schottky defects, the two most right columns of Table 2) turns α-AlB_2 unstable. But with increasing W content this impact is reversed, leading to more negative E_f values for defected α-$(W_{1-x}Al_x)_{1-y}B_{2(1-z)}$ (than defect-free α-$(W_{1-x}Al_x)_{1-y}B_{2(1-z)}$) if x is under

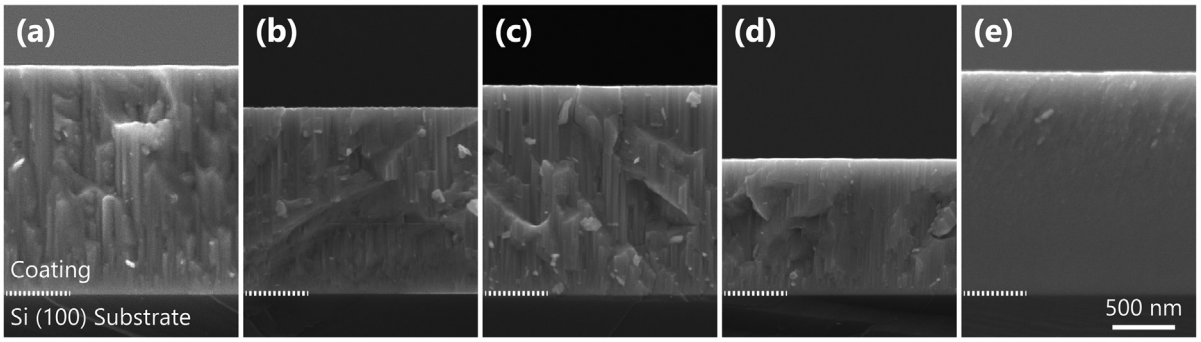

Fig. 3. SEM cross section micrographs of our thin films. The Al content increases from left to right, (a) was deposited with 7.4 W·cm^{-2} on the W_2B_{5-z} target and 0.0 W·cm^{-2} on the AlB_2 target, (b) with 7.4 and 3.7, (c) 7.4 and 7.4, (d) 3.7 and 7.4, and (e) with 1.9 and 7.4 W·cm^{-2} on the W_2B_{5-z} and AlB_2 target respectively. The dashed horizontal line, indicating the interface between film and Si substrate, has the same length as the 500-nm-scale bar.

Table 2
c-axis lattice parameter and E_f for binary α-AlB_2 and α -WB_2 with different vacancy concentrations. Note that a positive E_f means that the structure is unstable with respect to the elemental constituents.

M	MB_2	$MB_{1.9375}$	$M_{0.9375}B_2$	$M_{0.9375}B_{1.9375}$	$M_{0.9375}B_{1.875}$	$M_{0.875}B_{1.75}$
Al	3.30 Å	3.25 Å	3.26 Å	3.24 Å	3.24 Å	3.17 Å
	−0.044 eV/at	−0.0125 eV/at	−0.056 eV/at	−0.013 eV/at	+0.041 eV/at	+0.153 eV/at
W	3.40 Å	3.32 Å	3.32 Å	3.24 Å	3.25 Å	3.11 Å
	−0.055 eV/at	−0.088 eV/at	−0.096 eV/at	−0.133 eV/at	−0.141 eV/at	−0.165 eV/at

~0.6 (Fig. 4a). For α-WB_2 the impact of B and Me vacancies is similar, both lead to more negative E_f values. Hence, the formation of B vacancies, Me vacancies, as well as B and Me vacancies, is not penalized but even rewarded.

The combination of these effects (promotion of vacancies in the α-structure but penalization thereof in the ω-structure, especially on the W-rich side) leads to the result that the preference of the α-structure over the ω-structure shifts towards higher W-contents, if vacancies are considered. Indeed, while the ω-to α-transition of the defect-free phases is observed at about 40 at% W on the metal sublattice (indicated by the right dashed vertical line in Fig. 4a)—in agreement with recent calculations for increased supercell sizes [13]—all three vacancy types (metal vacancy, boron vacancy and metal plus boron vacancy), shift the transition clearly to the W-rich side, to ~60 at% W for the Me and B vacancy containing structures considered here (indicated by the left dashed vertical line in Fig. 4a). The shift of the ω to α transition to higher W concentrations with increasing vacancy content is nicely represented by the distance of the two dashed vertical lines (Fig. 4a), which emphasizes the importance of point defects such as vacancies on the phase stability.

The fact that all of our crystalline films crystallize in the α structure suggests the presence of even higher defect concentrations as considered within Fig. 4a. For example, when considering 12.5% Schottky defects, the energy of formation of α-WB_2 is with −0.165 eV/at (Table 2) already more negative than that of ω-W_2B_{5-z} (E_f^{α} - E_f^{ω} is +0.26 eV/at for defect-free WB_2 and only +0.063 eV/at for 6.25% Schottky defect containing WB_2).

For W-metal-fractions below 40 at% not just the energy of formation is always more positive for the ω-phase than for the α-phase, but it is also rather close to zero (if not even positive) for B vacancy containing as well as B and Me vacancy containing Al-rich structures. This agrees with our experiments showing that Al-rich $(W_{1-x}Al_x)_{1-y}B_{2(1-z)}$ thin films always became X-ray amorphous, and no crystalline AlB_2 film could be realized so far (in its as deposited state).

In principle, the ab initio calculations predict the formation of the ω-phase for a broad compositional range for defect-free and low vacancy containing $(W_{1-x}Al_x)_{1-y}B_{2(1-z)}$, thus holding as explanation for the formation of ω-$Al_{0.50}W_{0.50}B_2$ under annealing of the amorphous thin film: here the film (*i.e.* the crystalline parts inside the film) forms rather under equilibrium like conditions, such that potentially less defects are created during crystal formation, being a prerequisite for the formation of the ω-phase.

In Fig. 4b we depict the energy of formation for α-$(W_{1-x}Al_x)_{1-y}B_{2(1-z)}$ without (y = 0, z = 0) and with Schottky defects (6.25%, *i.e.* y = 0.0625, z = 0.625), indicated by the diamond and asterisk symbols, respectively. Consequently, both cases correspond to stoichiometric compounds. We immediately observe that especially the W-rich side even promotes the formation of Schottky defects. On the Al-rich side (W-metal-fractions below 0.5), clearly the defect-free structure is most stable. This indicates that vacancy containing single-phase ternary $(W_{1-x}Al_x)_{1-y}B_{2(1-z)}$ PVD thin films (as observed in our experiments) decompose upon annealing towards vacancy-containing W-rich phases and nearly vacancy-free Al-rich phases. Such a scenario is also indicated in Fig. 4b. Moreover, several compositions were calculated twice with different positions of the considered vacancies in the crystal lattice (Al-near and W-near) which again highlights the preference of vacancies towards the W-rich regions.

Thus, the experimentally observed decomposition of our as deposited single-phase α-$W_{0.81}Al_{0.19}B_2$ thin film upon annealing at 1000 °C for 30 min, points towards a spinodal decomposition to form vacancy-free Al-rich domains and defected W-rich domains.

Besides an isostructural spinodal decomposition, a second decomposition pathway is conceivable, as especially the W-rich domains (which would prefer the ω-type for lower vacancy concentrations) could also form an intermediate phase (between the α-type and ω-type). Such an intermediate phase (*i.e.* a transition from α to ω via a continuous transformation of flat to puckered B-planes) could be seen as a mixture of α- and ω-type or an intermediate structure with *e.g.* two puckered and four flat boron layers (here simply denoted as μ-type). The formation of such an intermediate phase during decomposition would yield a higher energy gain as puckered layers are energetically favorable for the W-rich part (see the red hexagon in Fig. 4a), with E_f of −0.23 eV.

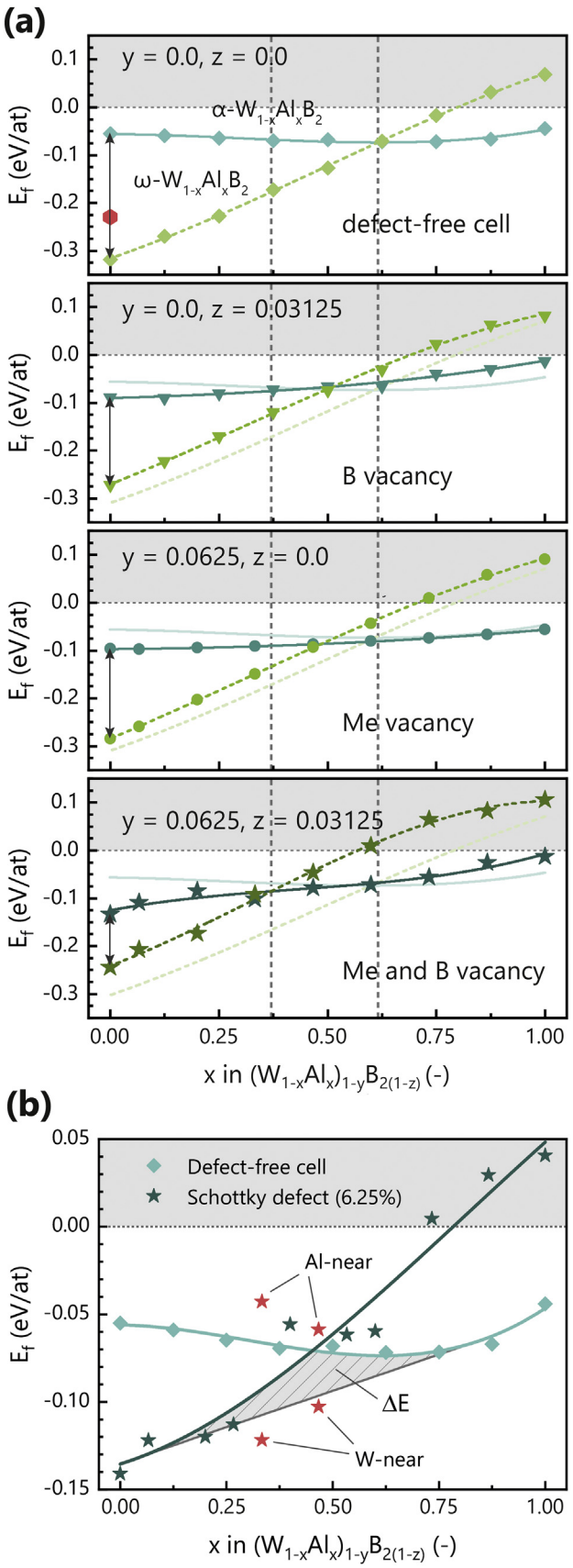

Fig. 4. (a) Energy of formation for different vacancy concentrations of α-$(W_{1-x}Al_x)_{1-y}B_{2(1-z)}$ (solid lines) and ω-$(W_{1-x}Al_x)_{1-y}B_{2(1-z)}$ (dashed lines), as function of the Al metal fraction x = Al/(Al + W). The dashed vertical lines indicate the position of the α to ω transition for crystals without vacancies (right dashed line) and with Me and B vacancy (left dashed line). The transparent lines shown in the second, third, and fourth panel are the normalized (with regard to chemical composition) data of the first panel (for defect-free cells), providing an overview on the trends. The red hexagon denotes an intermediate phase between α-WB_2 and ω-W_2B_{5-z}, consisting of two puckered and four flat boron layers. (b) shows a possible scenario for the decomposition of the experimentally observed $(W_{0.81}Al_{0.19})_{1-y}B_{2-z}$ coating into defect-free Al rich (Al,W)B_2 and defected W-rich (W,Al)B_2. The consequential minimum energy gain is marked as grey area. The red asterisks denote variations in the vacancy distribution (near the W-atom or the Al-atom). (For interpretation of the references to color in this figure legend, the reader is referred to the Web version of this article.)

The above discussion has its focus on the energy of formation and completely neglects entropic contributions to the phase stability. Due to the configurational entropy being a function of the chemical composition, meaning equivalent entropic contributions for both structural modifications of $(W_{1-x}Al_x)_{1-y}B_{2(1-z)}$, it will not affect the composition at which the transition takes place. The vibrational entropy on the other hand, may in principle be different for both modifications, however due to their structural similarity, these differences are expected to become significant only at strongly elevated temperatures. Yet, vacancy containing structures on the other hand may indeed be stabilized by entropy at elevated temperatures.

To investigate the finding that vacancies have especially in the α-structure a different impact on Al-rich or W-rich phases, we have analyzed the electronic density of states (DOS) for different vacancy contents of α-structured AlB_2 and WB_2. Indeed, both phases α-AlB_2 and α-WB_2, show a pseudogap in their DOS, which, for the stoichiometric compound, lies below the Fermi level (see Fig. 5). For AlB_2 the pseudogap is only slightly below the Fermi level (E_F), such that introducing vacancies on the metal sublattice indeed moves E_F into the pseudogap, while the DOS otherwise remains rather unchanged. This corresponds to what we would expect from a rigid band model by removing electrons from the system. These findings moreover indicate that for a stoichiometry close to $Al_{0.9375}B_2$ an electronic stabilization of the structure can be expected with the Fermi energy lying in the pseudogap. This is in good agreement with experimental and theoretical work on bulk AlB_2 where stoichiometries of about $Al_{0.9}B_2$ have been proposed [44,45]. For vacancies on the boron sublattice on the other hand, the Fermi level also comes close to the pseudogap, however, the number of states around the Fermi energy is clearly increased, indicating a change in the band structure, going along with a destabilization due to additional anti-bonding states (Fig. 5). Note that the value at E_F is almost the same, but in case of the defect-free structure, the number of states below E_F (antibonding states) decreases, whereas it increases for the boron substoichiometry. Interestingly, further vacancies indeed render the AlB_2 system unstable with respect to decomposition in fcc-Al and α-boron (see E_f in Table 2). This is also clearly visible from the DOS for the case of one metal and two boron vacancies (a Schottky defect, for our supercells used, this is equivalent to 6.25% Schottky defects), which is also depicted in Fig. 5. Here, a significant increase in states in the antibonding region close to E_F is observed. Similarly, we also have studied the effect of vacancies on the electronic structure of α-WB_2. Now, we find the structure to be highly tolerant with respect to metal and boron vacancies. In fact, with increasing vacancy content the DOS at the Fermi level is gradually decreasing, such that we indeed see an electronic stabilization of the structure. Interestingly, we find that structures with stoichiometric vacancy distribution over the two sublattices (Schottky defects, *i.e.* $(W_{1-x}Al_x)_{1-y}B_{2(1-z)}$ with z = 0.03125 and 0.0625) are more stable than defect-free α-WB_2 in agreement to our previous study [16]. This means that while α-AlB_2 tolerates only a small vacancy content on the metal sublattice, α-WB_2 is electronically stabilized by higher vacancy concentrations

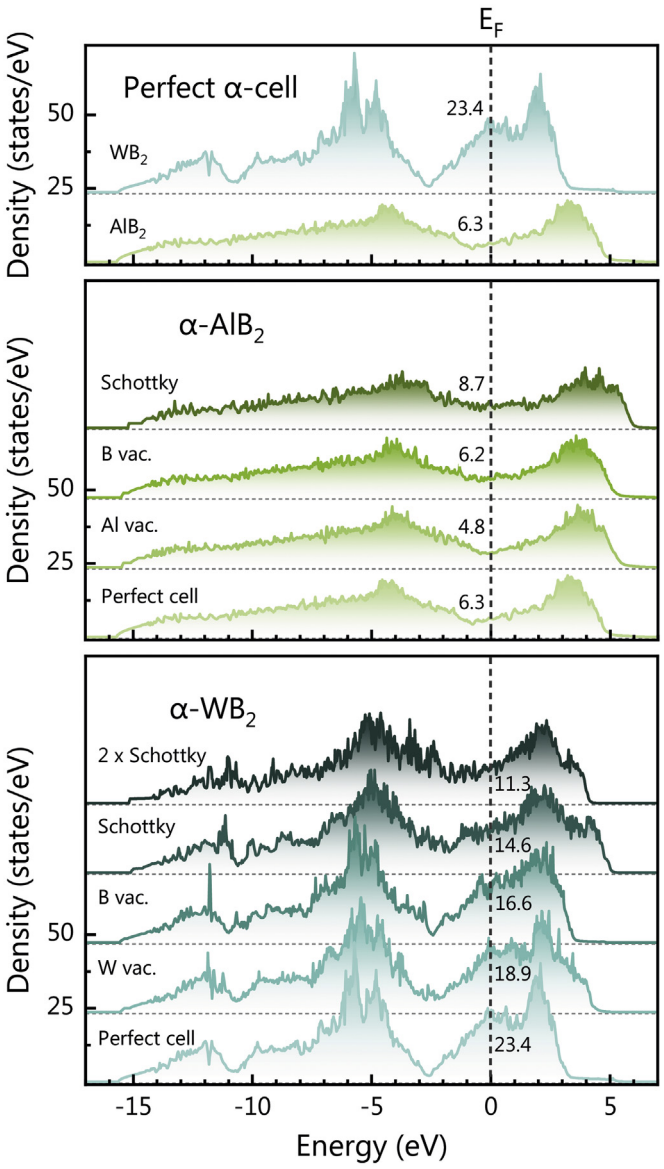

Fig. 5. DOS for different vacancy configurations of α-AlB_2 and α-WB_2. The values besides the dashed line showing the Fermi-level indicate the number of states at the Fermi energy.

on both sublattices. Finally, we need to mention that the samples showed a significant difference in their oxidation stability if containing Al or not. The Al-free WB_2 coatings showed already after 1 week of ambient air exposure a change of their color towards greenish appearance, indicating ongoing oxidation processes. Contrary, the Al-containing samples (even if only 2.3 at% at the metal sublattice) did not show such a change.

4. Summary and conclusion

Making use of the interplay between two different polymorphs has been shown to result in materials with improved mechanical properties. Especially in the well-known $Ti_{1-x}Al_xN$ system metastable cubic solid solutions have shown significantly improved hardness and better ductility. Similarly, we show here that WB_2 can be alloyed with up to 20 at% Al metal-fraction without significant performance loss, pointing to an increased oxidation stability due to Al, as one would expect the formation of an Al-oxide passivation layer. This, however, has to be further investigated. Hence, the main advantage of Al addition to WB_2 thin films is a self-passivation at ambient conditions, as well as an increased oxidation resistance in possible future applications. Unfortunately, a further increase of the Al-content to the Al-rich side could be shown to be difficult, which is especially due to the destabilizing nature of boron vacancies. This leaves us with an interesting situation: While vacancies electronically stabilize the α-over the ω-phase for high W contents, they at the same time destabilize the α-phase at high Al contents, making it difficult to grow crystalline α-AlB_2 by PVD (with their typically high fraction of point defects). This once more points to the importance of point defects for stability and mechanical properties of PVD deposited coatings, a fact that is now also understood to be crucial for boride-based coatings.

Acknowledgment

We thank Dr. Helmut Riedl and Dr. Matthias Bartosik for fruitful discussions on thin film deposition and XRD analysis. We thank the Vienna Scientific Cluster for the attribution of computation time, the center for transmission electron microscopy of TU Wien (USTEM) for providing the SEM, and the X-ray center of TU Wien for beam time. The present study was partly held within START Project (Y371) of the Austrian Science Fund. The financial support by the Austrian Federal Ministry of Economy, Family and Youth and the National Foundation for Research, Technology and Development is greatly acknowledged. We also thank Oerlikon Surface Solutions AG and Plansee Composite Materials GmbH for the financial support.

References

[1] P.H. Mayrhofer, C. Mitterer, L. Hultman, H. Clemens, Microstructural design of hard coatings, Prog. Mater. Sci. 51 (2006) 1032–1114, https://doi.org/10.1016/j.pmatsci.2006.02.002.
[2] R. Hahn, M. Bartosik, R. Soler, C. Kirchlechner, G. Dehm, P.H. Mayrhofer, Superlattice effect for enhanced fracture toughness of hard coatings, Scripta Mater. 124 (2016), https://doi.org/10.1016/j.scriptamat.2016.06.030.
[3] H. Riedl, A. Vieweg, A. Limbeck, J. Kalaš, M. Arndt, P. Polcik, H. Euchner, M. Bartosik, P.H. Mayrhofer, Thermal stability and mechanical properties of boron enhanced Mo-Si coatings, Surf. Coating. Technol. (2015), https://doi.org/10.1016/j.surfcoat.2015.09.015.
[4] P.H. Mayrhofer, D. Music, J.M. Schneider, Ab initio calculated binodal and spinodal of cubic Ti1−xAlxN, Appl. Phys. Lett. 88 (2006) 071922, https://doi.org/10.1063/1.2177630.
[5] P.H. Mayrhofer, L. Hultman, J.M. Schneider, P. Staron, H. Clemens, Spinodal decomposition of cubic Ti1-xAlxN: comparison between experiments and modeling, Int. J. Mater. Res. 98 (2007) 1054–1059, https://doi.org/10.3139/146.101570.
[6] R. Rachbauer, S. Massl, E. Stergar, D. Holec, D. Kiener, J. Keckes, J. Patscheider, M. Stiefel, H. Leitner, P.H. Mayrhofer, Decomposition pathways in age hardening of Ti-Al-N films, J. Appl. Phys. (2011), https://doi.org/10.1063/1.3610451.
[7] P.H. Mayrhofer, A. Hörling, L. Karlsson, J. Sjölén, T. Larsson, C. Mitterer, L. Hultman, Self-organized nanostructures in the Ti-Al-N system, Appl. Phys. Lett. 83 (2003) 2049–2051, https://doi.org/10.1063/1.1608464.
[8] A. Hörling, L. Hultman, M. Odén, J. Sjölén, L. Karlsson, Thermal stability of arc evaporated high aluminum-content Ti1−xAlxN thin films, J. Vac. Sci. Technol. A Vacuum, Surfaces, Film. 20 (2002) 1815–1823, https://doi.org/10.1116/1.1503784.
[9] M. Schlögl, C. Kirchlechner, J. Paulitsch, J. Keckes, P.H. Mayrhofer, Effects of structure and interfaces on fracture toughness of CrN/AlN multilayer coatings, Scripta Mater. 68 (2013) 917–920, https://doi.org/10.1016/j.scriptamat.2013.01.039.
[10] M. Bartosik, C. Rumeau, R. Hahn, Z.L. Zhang, P.H. Mayrhofer, Fracture toughness and structural evolution in the TiAlN system upon annealing, Sci. Rep. 7 (2017) 16476, https://doi.org/10.1038/s41598-017-16751-1.
[11] M. Bartosik, H.J. Böhm, C. Krywka, Z.L. Zhang, P.H. Mayrhofer, Influence of phase transformation on the damage tolerance of Ti-Al-N coatings, Vacuum (2018), https://doi.org/10.1016/j.vacuum.2018.06.001.
[12] H. Euchner, P.H. Mayrhofer, Designing thin film materials — ternary borides from first principles, Thin Solid Films 583 (2015) 46–49, https://doi.org/10.1016/j.tsf.2015.03.035.
[13] H. Euchner, P.H. Mayrhofer, H. Riedl, F.F. Klimashin, A. Limbeck, P. Polcik, S. Kolozsvari, Solid solution hardening of vacancy stabilized TixW1−xB2, Acta Mater. 101 (2015) 55–61. https://doi.org/10.1016/j.actamat.2015.08.048.

[14] O.V. Sobol, O.N. Grigoryev, Y.A. Kunitsky, S.N. Dub, A.A. Podtelezhnikov, A.N. Stetsenko, Peculiarities of structure state and mechanical characteristics in ion-plasma condensates of quasibinary system borides W2B5-TiB2, Sci. Sinter. (2006), https://doi.org/10.2298/SOS0601063S.
[15] B. Alling, H. Högberg, R. Armiento, J. Rosen, L. Hultman, A theoretical investigation of mixing thermodynamics, age-hardening potential, and electronic structure of ternary $M^{1<}$inf>1-x$M^{2<}$inf>xB_2 alloys with AlB_2 type structure, Sci. Rep. (2015), https://doi.org/10.1038/srep09888.
[16] C. Fuger, V. Moraes, R. Hahn, H. Bolvardi, P. Polcik, H. Riedl, P.H. Mayrhofer, Influence of Tantalum on phase stability and mechanical properties of WB $_2$, MRS Commun (2019) 1–6, https://doi.org/10.1557/mrc.2019.5.
[17] V. Moraes, C. Fuger, V. Paneta, D. Primetzhofer, P. Polcik, H. Bolvardi, M. Arndt, H. Riedl, P.H. Mayrhofer, Substoichiometry and tantalum dependent thermal stability of α-structured W-Ta-B thin films, Scripta Mater. 155 (2018) 5–10, https://doi.org/10.1016/J.SCRIPTAMAT.2018.06.005.
[18] P. Losbichler, C. Mitterer, Non-reactively sputtered TiN and TiB2 films: influence of activation energy on film growth, Surf. Coating. Technol. (1997), https://doi.org/10.1016/S0257-8972(97)00331-9.
[19] P.H. Mayrhofer, C. Mitterer, J.G. Wen, J.E. Greene, I. Petrov, Self-organized nanocolumnar structure in superhard TiB[sub 2] thin films, Appl. Phys. Lett. 86 (2005) 131909, https://doi.org/10.1063/1.1887824.
[20] V. Moraes, H. Riedl, C. Fuger, P. Polcik, H. Bolvardi, D. Holec, P.H. Mayrhofer, Ab initio inspired design of ternary boride thin films, Sci. Rep. (2018), https://doi.org/10.1038/s41598-018-27426-w.
[21] W. Hofmann, W. Jäniche, Der strukturtyp von Aluminiumborid (AlB2), Naturwissenschaften 23 (1935) 851.
[22] H.P. Woods, F.E. Wawner, B.G. Fox, Tungsten diboride: preparation and structure, Science (1966), https://doi.org/10.1126/science.151.3706.75.
[23] M. Frotscher, W. Klein, J. Bauer, M2B5 or M2B4 Reinvestigation of the Mo/B and W/B System, vol. 633, 2007, pp. 2626–2630.
[24] C. Jiang, Z. Pei, Y. Liu, J. Xiao, J. Gong, C. Sun, Preparation and characterization of superhard AlB 2 -type WB 2 nanocomposite coatings, Phys. Status Solidi 210 (2013) 1221–1227, https://doi.org/10.1002/pssa.201228828.
[25] Y.M. Liu, C.L. Jiang, Z.L. Pei, H. Lei, J. Gong, C. Sun, Microstructure and properties of AlB2-type WB2 thin films deposited by direct-current magnetron sputtering, Surf. Coating. Technol. 245 (2014) 108–116. https://doi.org/10.1016/j.surfcoat.2014.02.049.
[26] H. Euchner, P.H. Mayrhofer, Vacancy-dependent stability of cubic and wurtzite Ti1−xAlxN, Surf. Coating. Technol. 275 (2015) 214–218, https://doi.org/10.1016/j.surfcoat.2015.05.017.
[27] F.F. Klimashin, N. Koutná, H. Euchner, D. Holec, P.H. Mayrhofer, The impact of nitrogen content and vacancies on structure and mechanical properties of Mo-N thin films, J. Appl. Phys. (2016), https://doi.org/10.1063/1.4966664.
[28] P. Bliem, S. Mráz, S. Sen, O. Hunold, J.M. Schneider, Self-passivating (Re,Al)B2 coatings synthesized by magnetron sputtering,, Sci. Rep. 8 (2018) 15570, https://doi.org/10.1038/s41598-018-34042-1.
[29] I. Petrov, A. Hall, A.B. Mei, N. Nedfors, I. Zhirkov, J. Rosen, A. Reed, B. Howe, G. Greczynski, J. Birch, L. Hultman, J.E. Greene, Controlling the boron-to-titanium ratio in magnetron-sputter-deposited TiB x thin films, J. Vac. Sci. Technol. A Vacuum, Surfaces, Film. (2017), https://doi.org/10.1116/1.4982649.
[30] A. Cakara, M. Bonta, H. Riedl, P.H. Mayrhofer, A. Limbeck, Development of a multi-variate calibration approach for quantitative analysis of oxidation resistant Mo-Si-B coatings using laser ablation inductively coupled plasma mass spectrometry, Spectrochim. Acta Part B At. Spectrosc. (2016), https://doi.org/10.1016/j.sab.2016.04.004.
[31] W.D. Nix, Mechanical properties of thin films, Metall. Trans. A. 20 (1989) 2217–2245, https://doi.org/10.1007/BF02666659.
[32] G.M. Pharr, W.C. Oliver, Measurement of thin film mechanical properties using nanoindentation, MRS Bull. 17 (2013) 28–33, https://doi.org/10.1557/S0883769400041634.
[33] G. Kresse, J. Hafner, Ab-initio molecular dynamics for liquid metals, Phys. Rev. B 47 (1993) 558–561.
[34] G. Kresse, Efficient iterative schemes for ab initio total-energy calculations using a plane-wave basis set, Phys. Rev. B 54 (1996) 11169–11186, https://doi.org/10.1103/PhysRevB.54.11169.
[35] G. Kresse, J. Furthmüller, Efficiency of ab-initio total energy calculations for metals and semiconductors using a plane-wave basis set, Comput. Mater. Sci. (1996), https://doi.org/10.1016/0927-0256(96)00008-0.
[36] J.P. Perdew, Y. Wang, Accurate and simple analytic representation of the electron-gas correlation energy, Phys. Rev. B (1992), https://doi.org/10.1103/PhysRevB.45.13244.
[37] A. Zunger, S.H. Wei, L.G. Ferreira, J.E. Bernard, Special quasirandom structures, Phys. Rev. Lett. (1990), https://doi.org/10.1103/PhysRevLett.65.353.
[38] A. Van De Walle, P. Tiwary, M. De Jong, D.L. Olmsted, M. Asta, A. Dick, D. Shin, Y. Wang, L.Q. Chen, Z.K. Liu, Efficient stochastic generation of special quasirandom structures, Calphad Comput. Coupling Phase Diagrams Thermochem. (2013), https://doi.org/10.1016/j.calphad.2013.06.006.
[39] K. Momma, F. Izumi, VESTA 3 for three-dimensional visualization of crystal, volumetric and morphology data, J. Appl. Crystallogr. (2011), https://doi.org/10.1107/S0021889811038970.
[40] Powder Diffraction File 00-009-0154, International Center for Diffraction Data, 2011 (n.d.).
[41] Powder Diffraction File 00-006-0243, International Center for Diffraction Data, 2011 (n.d.).
[42] V. Moraes, C. Fuger, V. Paneta, D. Primetzhofer, P. Polcik, H. Bolvardi, M. Arndt, H. Riedl, P.H. Mayrhofer, Substoichiometry and tantalum dependent thermal stability of α-structured W-Ta-B thin films, Scripta Mater. 155 (2018) 5–10, https://doi.org/10.1016/j.scriptamat.2018.06.005.
[43] W. Hayami, A. Momozawa, S. Otani, Effect of defects in the formation of AlB2-Type WB2and MoB2, Inorg. Chem. 52 (2013) 7573–7577, https://doi.org/10.1021/ic400587j.
[44] U. Burkhardt, V. Gurin, F. Haarmann, H. Borrmann, W. Schnelle, A. Yaresko, Y. Grin, On the electronic and structural properties of aluminum diboride Al0.9B2, J. Solid State Chem. 177 (2004) 389–394. https://doi.org/10.1016/j.jssc.2002.12.001.
[45] I. Loa, K. Kunc, K. Syassen, P. Bouvier, Crystal structure and lattice dynamics of AlB2 under pressure and implications for MgB2, Phys. Rev. B Condens. Matter 66 (2002) 1–8, https://doi.org/10.1103/PhysRevB.66.134101.